

Deep Learning Method for Stationary Distribution of Reflected Brownian Motion

Jim Dai

Operations Research and Information Engineering, Cornell University, jd694@cornell.edu

Zhanhao Zhang

Operations Research and Information Engineering, Cornell University, zz564@cornell.edu

Abstract

The stationary distribution of reflected Brownian motion (RBM) plays an important role in the analysis of high-dimensional stochastic systems, yet closed-form solutions are known only for a few special cases. Computing important performance metrics, such as tail probabilities, is even more intractable, despite their practical relevance. In this paper, we develop a deep learning approach that accurately and efficiently learns the Laplace transform of high-dimensional RBMs based on the basic adjoint relationship (BAR). Our framework combines a careful design of the loss function, training data sampling procedure, and neural network architecture. We evaluate the proposed method on RBM instances with known ground-truth tail probabilities and demonstrate near-perfect prediction in high-dimensional settings, highlighting its potential as a general tool for analyzing stochastic systems beyond analytically tractable regimes. Our code can be found at <https://github.com/zhangz73/NN4MGF>.

1 Introduction

Reflected Brownian motion (RBM) plays an important role in the analysis of multiclass queueing networks, where it often arises as a diffusion approximation under heavy traffic. In such settings, the stationary distribution of an RBM provides useful approximations for the steady-state behavior of the underlying queueing network. Closed-form expressions for stationary distributions are known only for a few special classes of RBMs. This paper develops a scalable deep learning method for computing the Laplace transform of the stationary distribution of a high dimensional RBM. The computed Laplace transforms can be used to estimate tail probabilities that serve as important performance metrics, such as tail latency for queueing networks.

We consider a d -dimensional RBM $Z = \{Z(t), t \geq 0\}$ associated with data (Σ, μ, R) , which

satisfies the following equations:

$$\begin{aligned}
Z(t) &= Z(0) + X(t) + RY(t), & t \geq 0, \\
X &= \{X(t), t \geq 0\} \text{ is a } d\text{-dimensional Brownian motion with} \\
&\quad \text{covariance matrix } \Sigma \text{ and drift } \mu, \\
Y(0) &= 0, \quad Y(\cdot) \text{ is non-decreasing,} \\
\int_0^\infty Z_k(t) dY_k(t) &= 0, & k = 1, \dots, d.
\end{aligned}$$

The $d \times d$ matrix R is known as the reflection matrix. We assume that the RBM is well defined and has a unique stationary distribution π , which is satisfied, e.g., when R is an M -matrix and $R^{-1}\mu < 0$ (Harrison-Williams 1987). Define the Laplace transform of Z at steady state as

$$\begin{aligned}
\varphi_0(\theta) &= \mathbb{E}_\pi \left[e^{\langle -\theta, Z(0) \rangle} \right], & \theta \in \mathbb{R}_+^d \\
\varphi_k(\theta) &= \mathbb{E}_\pi \left[\int_0^1 e^{\langle -\theta, Z(t) \rangle} dY_k(t) \right], & k = 1, \dots, d,
\end{aligned}$$

where $Z(0)$ follows the stationary distribution π . Lemma 1 of [1] shows that the Laplace transforms φ and φ_k are uniquely characterized by the Laplace version of basic adjoint relationship (BAR)

$$\gamma_0(\theta)\varphi_0(\theta) = \sum_{k=1}^d \gamma_k(\theta)\varphi_k(\theta), \tag{1}$$

where $\gamma_0(\theta) = -\frac{1}{2}\langle \theta, \Sigma\theta \rangle + \langle \mu, \theta \rangle$ and $\gamma_k(\theta) = -\langle R^{(k)}, \theta \rangle$. Here, $R^{(k)}$ denotes the k -th column of R . In [1], the authors prove that the Laplace version BAR (1) is equivalent to the PDE version of the BAR that was first advanced in Harrison-Williams (1987).

In contrast to [2], which develops an efficient approach for estimating steady-state expectations of high-dimensional RBMs, our work targets the Laplace transforms of their stationary distributions. Since the Laplace transform can be numerically inverted to recover tail probabilities and, more broadly, the full stationary distribution [3], it provides a significantly richer characterization of system performance. To the best of our knowledge, this is the first framework for estimating the Laplace transform $\varphi_k(\cdot)$ of high-dimensional RBMs. The main methodological contribution is to turn the BAR characterization into a scalable learning problem by combining a carefully designed loss function tailored to the BAR and the structural properties of Laplace transforms, a targeted training data sampling scheme, and a neural network architecture whose number of trainable parameters does not scale with the dimension d . This yields an accurate and efficient computational tool for evaluating important performance metrics, such as tail probabilities and tail latencies, in large-scale stochastic systems beyond analytically tractable regimes.

Literature review. With the advancement of computational power, there has been growing interest in developing numerical methods for stochastic systems. For instance, [4] propose a deep

learning approach to compute convergence rates of Markov chains, and [5] extend this framework to estimate Lyapunov functions, solve Poisson equations, and approximate stationary distributions. However, these methods are currently limited to low-dimensional settings (e.g., two dimensions). Extending deep learning methods to high-dimensional stochastic systems remains significantly more challenging and has motivated a growing line of research in stochastic control and diffusion approximations.

Our work is closely related to this literature on applying deep learning to high-dimensional stochastic systems. In particular, the deep BSDE framework [6, 7] provides a powerful approach for solving high-dimensional stochastic control problems by leveraging connections between parabolic PDEs and backward stochastic differential equations. This framework has been successfully applied to a wide range of settings, including matching [8], scheduling [9], impulse control [10], drift control [11], and singular control [12]. Our work is also motivated by stochastic systems, as the equation (1) characterizes the stationary behavior of reflected Brownian motions. However, our setting is fundamentally different: unlike these approaches, which often exploit stochastic representations, such as the Feynman–Kac representation, to reformulate high-dimensional PDEs as stochastic differential equations, (1) describes a stationary relationship and does not admit such a reformulation.

Our work is also related to the extensive literature on applying deep learning to high-dimensional partial differential equations (PDEs); see the survey by [13]. In particular, prior work has studied PDEs arising from variational formulations using deep learning [14, 15, 16]. Our approach constructs a loss function based on the squared residual of (1), which parallels the least-squares formulations used in [14, 16]. However, directly minimizing this residual is insufficient in our setting due to generalizability and numerical stability issues. To address this, we design a structured loss function with additional regularization terms that enforce key properties of the Laplace transform. In addition, we propose a tailored sampling scheme and a neural network architecture that scale effectively to high-dimensional problems.

2 Deep learning approach

In this section, we approximate $\varphi_k(\cdot)$ for $k = 0, \dots, d$ in (1) using feedforward neural networks in the complex domain, where (1) continues to hold by analytic extension. Working in the complex domain is necessary because robust numerical inversion methods, such as the Talbot method [17] and related approaches [18, 19], evaluate the Laplace transform at complex arguments when computing tail probabilities. Let $\theta = \theta^{\text{Re}} + i\theta^{\text{Im}} \in \mathbb{C}^d$ be a d -dimensional complex vector, with $\theta^{\text{Re}}, \theta^{\text{Im}} \in \mathbb{R}^d$. We focus on accurate approximation over the bounded region

$$\Theta := [\underline{\theta}^{\text{Re}}, \bar{\theta}^{\text{Re}}]^d \times [-\bar{\theta}^{\text{Im}}, \bar{\theta}^{\text{Im}}]^d.$$

A naive approach is to use shallow feedforward neural networks to approximate the functions $\varphi_k(\cdot)$, and then update the network parameters by minimizing the mean-squared error between the left-

hand side and the right-hand side of (1), where the training samples are drawn uniformly from Θ . This straightforward framework, however, suffers from several fundamental difficulties.

Poor generalization. The equation (1) characterizes the Laplace transform of the stationary distribution, which is analytic and monotone along the real axis. However, the naive training framework only minimizes a finite-sample residual of (1) and does not enforce either analyticity or monotonicity. As a result, the neural network may fit the sampled training points well while violating these structural properties and deviating significantly at unseen inputs.

Numerical stability. Because the Laplace transforms $\varphi_k(\theta)$ vary exponentially with θ , their values can differ by many orders of magnitude within $[\underline{\theta}, \bar{\theta}]^d$, leading to numerical precision issues when θ is either small or large.

Imbalanced training data. As d grows, samples drawn uniformly from high-dimensional boxes for the real and imaginary parts of θ rarely fall in corner regions, where many coordinates are simultaneously close to their extreme values. Instead, a typical sample contains a mixture of small and large coordinate values across dimensions. Consequently, the naive sampling scheme underrepresents regimes in which the Laplace transform exhibits large magnitudes or strong oscillatory behavior, making it difficult for the training algorithm to learn these regions accurately.

Poor scalability. A standard feedforward network takes the full vector $\theta \in \mathbb{C}^d$ as input, so the size of its input layer grows linearly with d . As a result, the first layer contains parameters tied to individual input coordinates, which must be learned from samples that capture sufficient variability of θ across all d dimensions. As d increases, achieving such coverage requires substantially larger sample sizes, making the naive architecture less scalable for high-dimensional RBMs.

In the rest of this section, we will describe how we address these issues through a careful design of the loss function, training data sampling, and neural network architecture.

2.1 Loss function

Instead of directly learning the Laplace transforms $\varphi_k(\cdot)$, we parameterize their logarithms using neural networks. Specifically, the networks output functions $f_k(\cdot)$ such that

$$\varphi_k(\theta) = \exp(f_k(\theta)), \quad k = 0, \dots, d.$$

This log-parameterization improves numerical stability and allows us to work with quantities of comparable scale when evaluating the BAR equation.

For any $\theta \in \Theta$, we define the loss function

$$\begin{aligned} \mathcal{L}(\theta) := & \mathcal{L}_{\text{BAR}}(\theta) + \lambda_{\text{pair}} \cdot \mathcal{L}_{\text{pair}}(\theta) + \lambda_{\text{mono}} \cdot \mathcal{L}_{\text{mono}}(\theta) \\ & + \lambda_{\text{CR}} \cdot \mathcal{L}_{\text{CR}}(\theta) + \lambda_{\text{zero}} \cdot \mathcal{L}_{\text{zero}}, \end{aligned} \tag{2}$$

where $\lambda_{\text{pair}}, \lambda_{\text{mono}}, \lambda_{\text{CR}}, \lambda_{\text{zero}} > 0$ are hyperparameters that balance the relative importance of the different loss components. The first term enforces the BAR equation, while the remaining terms incorporate structural properties that the Laplace transforms are known to satisfy.

2.1.1 Normalized BAR error.

The primary objective is to enforce the BAR equation (1). However, directly comparing the two sides of the equation can lead to numerical instability because the Laplace transforms may vary exponentially with θ . To mitigate this issue, we introduce a normalization factor.

For any input $\theta \in \Theta$, we first compute the normalization factor $\nu(\theta)$ as:

$$\nu(\theta) := \max_{k=0, \dots, d} \{ \log |\gamma_k(\theta)| + f_k^{\text{Re}}(\theta) \}.$$

This normalization rescales the two sides of the BAR equation to a comparable magnitude before evaluating their difference. We then compute

$$\begin{aligned} \kappa_l(\theta) &= \gamma_0(\theta) \cdot \exp \left(f_0(\theta) - \nu(\theta) \right), \\ \kappa_r(\theta) &= \sum_{k=1}^d \gamma_k(\theta) \cdot \exp \left(f_k(\theta) - \nu(\theta) \right). \end{aligned}$$

Finally, the normalized BAR error is given as

$$\mathcal{L}_{\text{BAR}}(\theta) := \left(\frac{|\kappa_l(\theta) - \kappa_r(\theta)|}{|\kappa_l(\theta)| + |\kappa_r(\theta)| + \epsilon} \right)^2, \quad (3)$$

where $\epsilon > 0$ is a very small constant to avoid division by zero. This normalized error stabilizes training by comparing the relative discrepancy between the two sides of (1).

2.1.2 Pairwise consistency penalty.

Next, we exploit structural constraints implied by the BAR equation by constructing points at which only one boundary term remains active. Given input $\theta \in \Theta$, we construct $\tilde{\theta}^{(1)}, \dots, \tilde{\theta}^{(d)}$ that satisfies $R_{-k} \tilde{\theta}^{(k)} = 0$ and $\tilde{\theta}_k^{(k)} = \theta_k$, where R_{-k} denotes the matrix obtained from R by removing its k -th row. By construction, these vectors lie on the boundary where only one reflection term remains active. In particular, for any $k, k' = 1, \dots, d$ such that $k \neq k'$, we have $\gamma_{k'}(\tilde{\theta}^{(k)}) = 0$.

The original BAR equation relates the interior function only to the aggregate contribution of all boundary functions. Consequently, each boundary function is constrained only indirectly through this aggregate residual, making it difficult to learn the individual boundary functions efficiently. We therefore use the constructed points above to directly relate each boundary function to the interior function, providing an explicit constraint for each individual boundary function. Substituting this relation into (1) and taking logarithms yields the following pairwise consistency penalty, which substantially accelerates convergence:

$$\mathcal{L}_{\text{pair}}(\theta) := \sum_{k=1}^d \left(\log \gamma_0(\tilde{\theta}^{(k)}) + f_0(\tilde{\theta}^{(k)}) - \log \gamma_k(\tilde{\theta}^{(k)}) - f_k(\tilde{\theta}^{(k)}) \right)^2. \quad (4)$$

2.1.3 Monotonicity penalty.

The Laplace transforms are non-increasing in the real part of θ . To enforce this property in the learned functions, we introduce a monotonicity penalty. Given any input $\theta \in \Theta$, we construct $\tilde{\theta} := \text{Re}(\theta) + 0i$, which lies on the real axis.

$$\mathcal{L}_{\text{mono}}(\theta) := \sum_{k=0}^d \left(\frac{\partial f_k^{\text{Re}}(\tilde{\theta})}{\partial \text{Re}(\tilde{\theta})} \right)^+ + \lambda_{\text{img}} \sum_{k=0}^d (f_k^{\text{Im}}(\tilde{\theta}))^2, \quad (5)$$

where $\lambda_{\text{img}} > 0$ is a hyperparameter. The first term penalizes violations of monotonicity, while the second enforces real-valued outputs when θ lies on the real axis.

2.1.4 Cauchy-Riemann penalty.

Since the Laplace transforms are analytic functions, their real and imaginary parts must satisfy the Cauchy–Riemann equations. We therefore include the following penalty to enforce approximate analyticity:

$$\mathcal{L}_{\text{CR}}(\theta) := \sum_{k=0}^d \left[\left(\frac{\partial f_k^{\text{Re}}(\theta)}{\partial \text{Re}(\theta)} - \frac{\partial f_k^{\text{Im}}(\theta)}{\partial \text{Im}(\theta)} \right)^2 + \left(\frac{\partial f_k^{\text{Re}}(\theta)}{\partial \text{Im}(\theta)} + \frac{\partial f_k^{\text{Im}}(\theta)}{\partial \text{Re}(\theta)} \right)^2 \right]. \quad (6)$$

2.1.5 Zero-anchoring penalty.

Finally, we anchor the interior transform at the origin. Since $\varphi_0(0) = 1$, we enforce this normalization through

$$\mathcal{L}_{\text{zero}} := \|\exp(f_0(0)) - 1\|_2^2. \quad (7)$$

2.2 Sampling strategy

At each gradient update for minimizing the loss function (2), we sample a batch of N data points from Θ to compute the loss and its gradient with respect to the neural network parameters. As discussed above, uniform sampling becomes increasingly ineffective in high dimensions because it rarely samples targeted corner regions. These regions are important for capturing large-magnitude Laplace values in the real domain and strong oscillatory behavior in the imaginary domain, both of which can significantly affect the accuracy of numerical inversion methods such as the Talbot method. To improve coverage of these regions while maintaining support over the full domain Θ , we adopt the following two-stage sampling procedure.

We sample each training data point $\theta \in \Theta$ in a batch as follows:

- Step 1:** We first sample scalar reference thresholds $\theta_*^{\text{Re}} \sim \text{Unif}[\underline{\theta}^{\text{Re}}, \bar{\theta}^{\text{Re}}]$ and $\theta_*^{\text{Im}} \sim \text{Unif}[0, \bar{\theta}^{\text{Im}}]$. These thresholds determine the targeted corner regions for the real and imaginary parts.

2. **Step 2:** Conditional on these thresholds, we sample $\theta^{\text{Re}} \sim \text{Unif}[\underline{\theta}^{\text{Re}}, \theta_*^{\text{Re}}]^d$ and $\theta^{\text{Im}} \sim \text{Unif}([[-\bar{\theta}^{\text{Im}}, -\theta_*^{\text{Im}}] \cup [\theta_*^{\text{Im}}, \bar{\theta}^{\text{Im}}])^d$, and construct $\theta = \theta^{\text{Re}} + i\theta^{\text{Im}}$. This conditional sampling scheme increases the probability of drawing points near the lower corner of the real domain and near the outer corners of the imaginary domain.

We use this procedure to generate all training samples in each batch, with the batch size N chosen independently of the dimension d .

2.3 Neural network architecture

To address the scalability challenges discussed earlier, we design a neural network architecture whose size does not grow with the dimension d , which encodes each coordinate using a shared feature extractor and aggregates the resulting representations to produce the interior and boundary functions (see Figure 1a).

Shared coordinate encoder. Given $\theta = [\theta_1, \dots, \theta_d] \in \Theta$, we first apply a shared encoder to each coordinate θ_j , which combines two components (see Figure 1b). The first component computes Fourier features $\eta(\theta_j)$ of the real and imaginary parts of θ_j , which improves the ability of the network to represent oscillatory patterns. The second component maps the coordinate index j to an embedding vector z_j^{dim} , allowing the network to distinguish different coordinates while keeping the encoder weights shared across all dimensions.

Interior network. For each coordinate $j = 1, \dots, d$, the corresponding Fourier features $\eta(\theta_j)$ and the coordinate embedding vector z_j^{dim} are then passed to an interior network (i.e. a feedforward neural network with two heads) g_{int} . The network outputs a two-dimensional vector $g_{\text{int}}(\eta(\theta_j), z_j^{\text{dim}}) = (g_{\text{int}}^{\text{Re}}(\eta(\theta_j), z_j^{\text{dim}}), g_{\text{int}}^{\text{Im}}(\eta(\theta_j), z_j^{\text{dim}}))$, where $g_{\text{int}}^{\text{Re}}(\eta(\theta_j), z_j^{\text{dim}})$ (resp. $g_{\text{int}}^{\text{Im}}(\eta(\theta_j), z_j^{\text{dim}})$) represents the real (resp. imaginary) contribution of coordinate j to the log of the interior Laplace transform. These contributions are aggregated across coordinates to obtain $f_0^{\text{Re}}(\theta) = \sum_{j=1}^d g_{\text{int}}^{\text{Re}}(\eta(\theta_j), z_j^{\text{dim}})$ and $f_0^{\text{Im}}(\theta) = \sum_{j=1}^d g_{\text{int}}^{\text{Im}}(\eta(\theta_j), z_j^{\text{dim}})$. This additive structure allows the network to handle high-dimensional inputs while maintaining a parameter count that does not scale with d .

Shared boundary network. To represent the boundary functions, we use another feedforward network g_{bdary} with shared weights across all boundaries. For each boundary $k = 1, \dots, d$ and coordinate $j = 1, \dots, d$, in addition to the Fourier features $\eta(\theta_j)$ and the coordinate embedding vector z_j^{dim} , the network also receives a boundary index embedding z_k^{bdary} . The network outputs coordinate-wise contributions $g_{\text{bdary}}(\eta(\theta_j), z_j^{\text{dim}}, z_k^{\text{bdary}})$, which are again aggregated to produce $f_k^{\text{Re}}(\theta) = \sum_{j=1}^d g_{\text{bdary}}^{\text{Re}}(\eta(\theta_j), z_j^{\text{dim}}, z_k^{\text{bdary}})$ and $f_k^{\text{Im}}(\theta) = \sum_{j=1}^d g_{\text{bdary}}^{\text{Im}}(\eta(\theta_j), z_j^{\text{dim}}, z_k^{\text{bdary}})$ for $k = 1, \dots, d$.

Overall, this architecture leverages shared encoders and additive aggregation to achieve scalability in high dimensions while allowing the network to capture both interior and boundary behaviors

of the Laplace transforms.

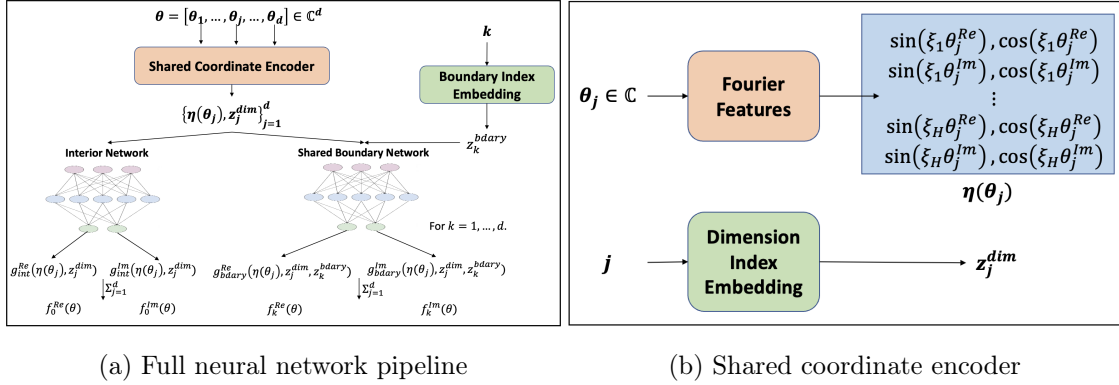


Figure 1: Neural network architecture

3 Numerical Experiments

We evaluate the performance of our neural network by estimating tail probabilities of the form $\mathbb{P}(\sum_j Z_j > t)$. The predicted probabilities are obtained by applying numerical inverse Laplace transforms using the Talbot method [17] to the Laplace transform learned by the neural network. To assess the accuracy of this approach, we consider two RBM examples for which ground truth results of tail probabilities can be obtained.

The first example is a 2-dimensional RBM from [20] and [21], which admits a closed-form expression for the stationary density but does not provide an explicit formula for the Laplace transform. In this case, we compute the ground-truth probabilities $\mathbb{P}(\sum_j Z_j > t)$ by numerically integrating the density function. The second and third examples are 20-dimensional and 30-dimensional RBMs from [1], whose Laplace transform admits a product-form expression. The corresponding ground-truth probabilities are computed by applying the same Talbot inversion method to the exact Laplace transform. Both numerical integration and Talbot inversion of Laplace transform can be achieved using the `mpmath` package in Python [22].

The predicted tail probabilities match the ground truth almost perfectly in both examples (see Figure 2). The two-dimensional example shows that our neural network can capture Laplace transforms with complex structures, where the behavior differs significantly across dimensions. The 20-dimensional and 30-dimensional examples highlight the scalability of the architecture: despite the high dimensionality, the neural network still produces highly accurate probability estimates. These results indicate that our neural network is both expressive enough to represent complex Laplace transforms and scalable to high-dimensional RBMs.

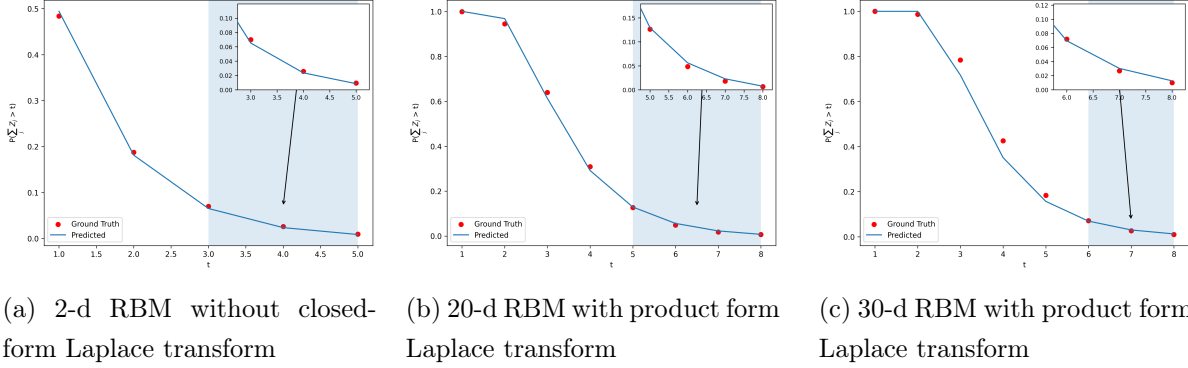


Figure 2: Tail probabilities (up to 1%) of the stationary sum $\sum_j Z_j$: neural network vs. ground truth.

4 Conclusion

In this paper, we propose a scalable deep learning framework for learning the Laplace transform of high-dimensional RBMs. Our approach integrates a carefully designed loss function, training data sampling procedure, and neural network architecture. Numerical experiments demonstrate that, by numerically inverting the learned Laplace transform, our method can accurately compute tail probabilities of the stationary distribution in high-dimensional settings. These results highlight the potential of our framework as a general tool for estimating performance metrics in large-scale stochastic systems.

Despite these promising results, several limitations remain. First, each gradient update currently requires 16,384 training samples, leading to substantial GPU memory usage when processed in a single batch, or increased runtime when split across multiple batches, as the dimension of the RBM grows. Developing more efficient training strategies to scale our approach to RBMs with hundreds or thousands of dimensions is an important direction for future work. Second, beyond RBMs, it would be of interest to extend our framework to broader classes of stochastic systems and estimate practically relevant performance metrics, such as tail latencies and throughput.

A Implementation Details

Construction of Fourier features. To enhance the representation of complex inputs, we employ Fourier feature embeddings applied separately to the real and imaginary parts. Consider an input $\theta := \theta^{\text{Re}} + i\theta^{\text{Im}} \in \mathbb{C}^d$. For each coordinate $j = 1, \dots, d$, we first normalize the inputs so that both the real and imaginary parts lie in $[-1, 1]$. Specifically, we define the normalized real and imaginary components $\tilde{\theta}_j^{\text{Re}}$ and $\tilde{\theta}_j^{\text{Im}}$ as

$$\begin{aligned}\tilde{\theta}_j^{\text{Re}} &:= 2 \frac{\theta_j^{\text{Re}} - \underline{\theta}_j^{\text{Re}}}{\bar{\theta}_j^{\text{Re}} - \underline{\theta}_j^{\text{Re}}} - 1, \\ \tilde{\theta}_j^{\text{Im}} &:= \frac{\theta_j^{\text{Im}} + \bar{\theta}_j^{\text{Im}}}{\bar{\theta}_j^{\text{Im}}} - 1.\end{aligned}$$

We then construct Fourier features based on these normalized inputs. Let H denote the total number of Fourier features for each of the real and imaginary parts, where H is assumed to be divisible by 2. We construct two sets of frequency grids $\{\xi_h^{\text{Re}}\}_{h=1}^{H/2}$ and $\{\xi_h^{\text{Im}}\}_{h=1}^{H/2}$ as fixed, non-trainable hyperparameters, using logarithmically spaced values over $[\delta_{\min}^{\text{Re}}, \delta_{\max}^{\text{Re}}]$ and $[\delta_{\min}^{\text{Im}}, \delta_{\max}^{\text{Im}}]$, respectively. The resulting $2H$ Fourier features are given by

$$\left\{ \sin\left(2\pi\xi_h^{\text{Re}}\theta_j^{\text{Re}}\right), \cos\left(2\pi\xi_h^{\text{Re}}\theta_j^{\text{Re}}\right), \sin\left(2\pi\xi_h^{\text{Im}}\theta_j^{\text{Im}}\right), \cos\left(2\pi\xi_h^{\text{Im}}\theta_j^{\text{Im}}\right) \right\}_{h=1, \dots, H/2}.$$

Hyperparameters for neural networks. In all experiments, we set $H = 64$, with $\delta_{\min}^{\text{Re}} = \delta_{\min}^{\text{Im}} = -4$, $\delta_{\max}^{\text{Re}} = 1$, and $\delta_{\max}^{\text{Im}} = 2$. The dimension index embedding z_j^{dim} and the boundary index embedding z_k^{bdary} are both chosen to have dimension 64. For the interior network and the shared boundary network, we use feedforward architectures with two hidden layers, each consisting of 128 neurons and SiLU activation.

Hyperparameters for training. For all experiments, we use the AdamW optimizer with a CosineAnnealing learning rate schedule, both implemented in PyTorch. The learning rate is initialized at 10^{-3} and annealed to 10^{-4} . We train the neural networks for 100,000 epochs, where each epoch corresponds to a single gradient update. For the 20- and 30-dimensional examples, we further fine-tune the neural networks for an additional 200,000 epochs. Specifically, the learning rate is annealed from 10^{-4} to 10^{-5} over the first 100,000 fine-tuning epochs, and then from 10^{-5} to 10^{-6} over the remaining 100,000 epochs. At each epoch, we sample $2^{14} = 16,384$ training data points to estimate the gradient of the loss function (2).

To reduce memory consumption, we evaluate the more expensive loss components (4)–(6) using random subsets of these 16,384 training data points. The pairwise consistency loss (4) is evaluated using only 300 points. This is because PyTorch stores the intermediate activations of the neural network for each input until backpropagation, and each input θ is transformed into d auxiliary inputs $\tilde{\theta}^{(1)}, \dots, \tilde{\theta}^{(d)}$, causing the memory requirement to grow linearly with d . For the monotonicity penalty

(5) and Cauchy–Riemann penalty (6), we first use 1024 points to evaluate the interior terms (i.e., $k = 0$), and then use 128 points to evaluate these penalties across all $k = 0, \dots, d$. These penalties are particularly memory intensive because they require first-order derivatives of the neural network outputs, which require retaining the computational graph so that gradients can be backpropagated through these derivatives. The penalty coefficients are set to $\lambda_{\text{bdary}} = \lambda_{\text{mono}} = \lambda_{\text{CR}} = 10$ and $\lambda_{\text{zero}} = 0.1$.

Problem instances. We consider two classes of RBMs for all our numerical experiments. The first is adopted from [20], where a closed-form expression is available for the stationary distribution, but not for its Laplace transform or tail probabilities. Specifically, we consider a 2-dimensional RBM with

$$\Sigma = \begin{bmatrix} 1 & 0 \\ 0 & 1 \end{bmatrix}, \quad \mu = \begin{bmatrix} -1 \\ 0 \end{bmatrix}, \quad R = \begin{bmatrix} 1 & 0 \\ -1 & 1 \end{bmatrix}.$$

The density ρ of its stationary distribution is given by

$$\rho(\theta) = Cr^{1/2}e^{-(r+\theta_1)} \cos(\psi/2),$$

where C , r , and ψ are defined as

$$\begin{aligned} C &= \frac{1}{\sqrt{\pi}} 2^{3/2}, \\ r &= \sqrt{\theta_1^2 + \theta_2^2}, \\ \psi &= \arccos(\theta_1/r). \end{aligned}$$

The tail probabilities are then obtained via numerical integration of ρ using `mpmath`.

The second class is adopted from [1], which admits a product-form Laplace transform due to the *skew-symmetry* property. An RBM is said to satisfy the skew-symmetry condition if

$$2\Sigma = R\text{diag}(R)^{-1}\text{diag}(\Sigma) + \text{diag}(\Sigma)\text{diag}(R)^{-1}R^T.$$

Following [1], we construct an RBM for any dimension $d \geq 2$ that satisfies the skew symmetry condition as follows:

$$\begin{aligned} R_{j,j} &= 1, & \forall j &= 1, \dots, d, \\ R_{j,j-1} &= -1, & \forall j &= 2, \dots, d, \\ \Sigma_{j,j} &= c_j + c_{j+1}, & \forall j &= 1, \dots, d, \\ \Sigma_{j,j-1} &= -c_j, & \forall j &= 2, \dots, d, \\ \Sigma_{j-1,j} &= -c_j, & \forall j &= 2, \dots, d, \\ \mu_j &= \beta_j - \beta_{j+1}, & \forall j &= 1, \dots, d, \end{aligned}$$

where the vectors $c \in \mathbb{R}^{d+1}$ and $\beta \in \mathbb{R}^{d+1}$ are defined by

$$\begin{aligned} c_j &= 1, & \forall j = 1, \dots, d+1, \\ \beta_j &= j, & \forall j = 1, \dots, d+1. \end{aligned}$$

According to [1], the corresponding Laplace transforms are given by

$$\begin{aligned} \varphi_0(\theta) &= \prod_{j=1}^d \frac{\alpha_j}{\alpha_j - \theta_j}, & \forall \theta < \alpha, \\ \varphi_k(\theta) &= \frac{\Sigma_{k,k}}{2R_{k,k}} \alpha_k \prod_{j \neq k} \frac{\alpha_j}{\alpha_j - \theta_j}, & \forall \theta < \alpha, \end{aligned}$$

where α is defined as

$$\alpha = -2\text{diag}(\Sigma)^{-1}\text{diag}(R)R^{-1}\mu.$$

The tail probabilities are then computed via numerical Laplace inversion using the Talbot method implemented in `mpmath`.

B Moments Estimation

B.1 Numerical procedure for computing moments given Laplace transform

Given the Laplace transform, we compute the moments of the RBM stationary distribution by following the procedure in [23]. To make this paper self-contained, we summarize the key steps below.

The method is based on numerical inversion of the Laplace transform in the complex plane. For each moment order n , the inversion is carried out along a circular contour

$$\mathcal{C}_n := \{z \in \mathbb{C} : |z| = r_n\},$$

centered at the origin with radius r_n . The contour integral representation of the moment is then approximated by evaluating the integrand at equally spaced points

$$z_j = r_n e^{i\pi j/(n\ell)}, \quad j = 0, 1, \dots, n\ell,$$

which leads to a trapezoidal-type discretization of the integral. This yields the following inversion formula:

$$m_n = \frac{n!}{2n\ell r_n^n a_n^n} \left[W_n(r_n) + (-1)^n W_n(-r_n) + 2 \sum_{j=1}^{n\ell-1} \text{Re}(W_n(z_j) e^{-i\pi j}) \right], \quad (8)$$

where $r_n = 10^{-\epsilon/(2n\ell)}$ for some accuracy parameter $\epsilon > 0$ and inversion parameter $\ell \in \{1, 2\}$. The parameter r_n is chosen to control the discretization error arising from approximating the contour

Algorithm 1: Adaptive moment computation from Laplace transform

Input : Laplace transform $\varphi(\theta)$, number of moments $M \geq 2$, accuracy parameter ϵ , inversion parameter $\ell \in \{1, 2\}$

// Step 1: Initial computation of m_1 and m_2

Set $a_1 \leftarrow 1$ and $a_2 \leftarrow m_1$

Compute m_1 and m_2 using (8) with $W_1(z) = \varphi(-a_1z)$ and $W_2(z) = \varphi(-a_2z)$

// Step 2: Refinement of m_1 and m_2

Set $a_1 \leftarrow \frac{2m_1}{m_2}$ and $a_2 \leftarrow \frac{2m_1}{m_2}$

Recompute m_1, m_2 using (8) with $W_1(z) = \varphi(-a_1z)$ and $W_2(z) = \varphi(-a_2z)$

// Step 3: Compute m_n for $3 \leq n \leq M$

for $n = 3, 4, \dots, M$ **do**

 Set $a_n \leftarrow \frac{(n-1)m_{n-2}}{m_{n-1}}$

 Compute m_n using (8) with $W_n(z) = \varphi(-a_nz)$

return m_1, m_2, \dots, m_M

integral using a finite trapezoidal sum, while the parameter ℓ helps mitigate round-off error by increasing the number of quadrature points along the contour. The function $W_n(z) := \varphi(-a_nz)$ is a rescaled version of the Laplace transform. The scaling factors $\{a_n\}$ are chosen adaptively so that the magnitude of $W_n(z)$ remains well-conditioned on the contour \mathcal{C}_n , preventing numerical overflow or underflow when computing high-order moments.

The overall procedure is summarized in Algorithm 1. It first computes the first two moments, refines them using improved scaling, and then proceeds recursively to higher-order moments using previously computed values to update the scaling factors.

B.2 Experiment results

Using the procedure described in Algorithm 1, we estimate the moments of RBMs adopted from [1] with dimensions 5, 20, and 30. The results are reported in Tables 1–3. Overall, the proposed framework provides accurate estimates for low-order moments, particularly in lower-dimensional settings. For the 5-dimensional RBM, the estimated first-, second-, and third-order moments all exhibit relatively small relative errors. For the 20- and 30-dimensional RBMs, the first-order moments also remain reasonably accurate across most coordinates. As the dimension and moment order increase, however, the estimation errors become larger, especially for certain second-order moments in the 30-dimensional case. This behavior is expected, as moment estimation relies on accurate local evaluations of the Laplace transform near $\theta = 0$ through contour-based derivative approximation, which becomes increasingly sensitive to approximation errors in high-dimensional settings. In contrast, the Talbot inversion used for tail probability estimation tends to remain more stable in high dimensions because it depends on evaluating the Laplace transform over a broader region of the complex plane rather than accurately recovering local derivative information near $\theta = 0$. As a result, small local

approximation errors are less significantly amplified compared with moment estimation.

First Moments				
Dimension j	True	Pred	Abs Err	Rel Err
0	1.00×10^0	9.98×10^{-1}	2.06×10^{-3}	2.06×10^{-3}
1	5.00×10^{-1}	4.99×10^{-1}	1.19×10^{-3}	2.38×10^{-3}
2	3.33×10^{-1}	3.34×10^{-1}	6.46×10^{-4}	1.94×10^{-3}
3	2.50×10^{-1}	2.51×10^{-1}	6.83×10^{-4}	2.73×10^{-3}
4	2.00×10^{-1}	2.00×10^{-1}	5.72×10^{-5}	2.86×10^{-4}
Second Moments				
0	2.00×10^0	2.00×10^0	3.09×10^{-3}	1.55×10^{-3}
1	5.00×10^{-1}	4.99×10^{-1}	8.76×10^{-4}	1.75×10^{-3}
2	2.22×10^{-1}	2.25×10^{-1}	2.28×10^{-3}	1.03×10^{-2}
3	1.25×10^{-1}	1.27×10^{-1}	2.18×10^{-3}	1.74×10^{-2}
4	8.00×10^{-2}	7.85×10^{-2}	1.45×10^{-3}	1.82×10^{-2}
Third Moments				
0	6.00×10^0	5.88×10^0	1.16×10^{-1}	1.93×10^{-2}
1	7.50×10^{-1}	7.27×10^{-1}	2.31×10^{-2}	3.08×10^{-2}
2	2.22×10^{-1}	2.27×10^{-1}	4.71×10^{-3}	2.12×10^{-2}
3	9.38×10^{-2}	9.60×10^{-2}	2.22×10^{-3}	2.36×10^{-2}
4	4.80×10^{-2}	4.32×10^{-2}	4.84×10^{-3}	1.01×10^{-1}

Table 1: Moment estimates for $d = 5$

First Moments				
Dimension j	True	Pred	Abs Err	Rel Err
0	1.00×10^0	9.90×10^{-1}	1.04×10^{-2}	1.04×10^{-2}
1	5.00×10^{-1}	4.75×10^{-1}	2.48×10^{-2}	4.97×10^{-2}
2	3.33×10^{-1}	3.19×10^{-1}	1.47×10^{-2}	4.42×10^{-2}
3	2.50×10^{-1}	2.37×10^{-1}	1.32×10^{-2}	5.28×10^{-2}
4	2.00×10^{-1}	1.88×10^{-1}	1.16×10^{-2}	5.81×10^{-2}
5	1.67×10^{-1}	1.53×10^{-1}	1.34×10^{-2}	8.02×10^{-2}
6	1.43×10^{-1}	1.32×10^{-1}	1.07×10^{-2}	7.52×10^{-2}
7	1.25×10^{-1}	1.17×10^{-1}	8.06×10^{-3}	6.45×10^{-2}
8	1.11×10^{-1}	1.04×10^{-1}	6.97×10^{-3}	6.27×10^{-2}
9	1.00×10^{-1}	9.29×10^{-2}	7.11×10^{-3}	7.11×10^{-2}
10	9.09×10^{-2}	8.54×10^{-2}	5.48×10^{-3}	6.03×10^{-2}
11	8.33×10^{-2}	7.79×10^{-2}	5.42×10^{-3}	6.51×10^{-2}

Dimension j	True	Pred	Abs Err	Rel Err
12	7.69×10^{-2}	7.22×10^{-2}	4.69×10^{-3}	6.09×10^{-2}
13	7.14×10^{-2}	6.72×10^{-2}	4.27×10^{-3}	5.98×10^{-2}
14	6.67×10^{-2}	6.23×10^{-2}	4.34×10^{-3}	6.51×10^{-2}
15	6.25×10^{-2}	5.87×10^{-2}	3.77×10^{-3}	6.03×10^{-2}
16	5.88×10^{-2}	5.58×10^{-2}	3.06×10^{-3}	5.20×10^{-2}
17	5.56×10^{-2}	5.32×10^{-2}	2.31×10^{-3}	4.16×10^{-2}
18	5.26×10^{-2}	5.07×10^{-2}	1.91×10^{-3}	3.64×10^{-2}
19	5.00×10^{-2}	4.82×10^{-2}	1.81×10^{-3}	3.62×10^{-2}
20	4.76×10^{-2}	4.60×10^{-2}	1.66×10^{-3}	3.49×10^{-2}
21	4.55×10^{-2}	4.42×10^{-2}	1.22×10^{-3}	2.67×10^{-2}
22	4.35×10^{-2}	4.26×10^{-2}	9.28×10^{-4}	2.13×10^{-2}
23	4.17×10^{-2}	4.06×10^{-2}	1.11×10^{-3}	2.67×10^{-2}
24	4.00×10^{-2}	3.89×10^{-2}	1.07×10^{-3}	2.68×10^{-2}
25	3.85×10^{-2}	3.74×10^{-2}	1.07×10^{-3}	2.78×10^{-2}
26	3.70×10^{-2}	3.60×10^{-2}	1.00×10^{-3}	2.71×10^{-2}
27	3.57×10^{-2}	3.51×10^{-2}	6.14×10^{-4}	1.72×10^{-2}
28	3.45×10^{-2}	3.34×10^{-2}	1.11×10^{-3}	3.23×10^{-2}
29	3.33×10^{-2}	3.23×10^{-2}	1.03×10^{-3}	3.08×10^{-2}

Second Moments

0	2.00×10^0	1.91×10^0	8.74×10^{-2}	4.37×10^{-2}
1	5.00×10^{-1}	4.50×10^{-1}	4.97×10^{-2}	9.93×10^{-2}
2	2.22×10^{-1}	2.07×10^{-1}	1.50×10^{-2}	6.77×10^{-2}
3	1.25×10^{-1}	1.18×10^{-1}	6.76×10^{-3}	5.41×10^{-2}
4	8.00×10^{-2}	7.47×10^{-2}	5.33×10^{-3}	6.67×10^{-2}
5	5.56×10^{-2}	4.86×10^{-2}	6.97×10^{-3}	1.25×10^{-1}
6	4.08×10^{-2}	3.44×10^{-2}	6.39×10^{-3}	1.57×10^{-1}
7	3.13×10^{-2}	1.85×10^{-2}	1.28×10^{-2}	4.09×10^{-1}
8	2.47×10^{-2}	2.07×10^{-2}	4.04×10^{-3}	1.64×10^{-1}
9	2.00×10^{-2}	1.26×10^{-2}	7.42×10^{-3}	3.71×10^{-1}
10	1.65×10^{-2}	9.04×10^{-3}	7.49×10^{-3}	4.53×10^{-1}
11	1.39×10^{-2}	8.66×10^{-3}	5.23×10^{-3}	3.77×10^{-1}
12	1.18×10^{-2}	-2.12×10^{-3}	1.40×10^{-2}	1.18×10^0
13	1.02×10^{-2}	2.56×10^{-3}	7.65×10^{-3}	7.49×10^{-1}
14	8.89×10^{-3}	2.26×10^{-3}	6.63×10^{-3}	7.45×10^{-1}
15	7.81×10^{-3}	6.45×10^{-3}	1.37×10^{-3}	1.75×10^{-1}
16	6.92×10^{-3}	5.53×10^{-3}	1.39×10^{-3}	2.01×10^{-1}
17	6.17×10^{-3}	3.53×10^{-3}	2.64×10^{-3}	4.28×10^{-1}
18	5.54×10^{-3}	2.21×10^{-3}	3.33×10^{-3}	6.01×10^{-1}
19	5.00×10^{-3}	4.34×10^{-3}	6.56×10^{-4}	1.31×10^{-1}
20	4.54×10^{-3}	-3.56×10^{-3}	8.09×10^{-3}	1.78×10^0
21	4.13×10^{-3}	-3.49×10^{-4}	4.48×10^{-3}	1.08×10^0

Dimension j	True	Pred	Abs Err	Rel Err
22	3.78×10^{-3}	-6.16×10^{-4}	4.40×10^{-3}	1.16×10^0
23	3.47×10^{-3}	9.72×10^{-5}	3.38×10^{-3}	9.72×10^{-1}
24	3.20×10^{-3}	-2.92×10^{-3}	6.12×10^{-3}	1.91×10^0
25	2.96×10^{-3}	-2.83×10^{-3}	5.79×10^{-3}	1.96×10^0
26	2.74×10^{-3}	-3.85×10^{-3}	6.60×10^{-3}	2.40×10^0
27	2.55×10^{-3}	8.05×10^{-5}	2.47×10^{-3}	9.68×10^{-1}
28	2.38×10^{-3}	1.71×10^{-3}	6.69×10^{-4}	2.81×10^{-1}
29	2.22×10^{-3}	1.58×10^{-3}	6.43×10^{-4}	2.89×10^{-1}

Table 3: Moment estimates for $d = 30$

First Moments				
Dimension j	True	Pred	Abs Err	Rel Err
0	1.00×10^0	9.94×10^{-1}	5.84×10^{-3}	5.84×10^{-3}
1	5.00×10^{-1}	4.89×10^{-1}	1.10×10^{-2}	2.20×10^{-2}
2	3.33×10^{-1}	3.28×10^{-1}	5.17×10^{-3}	1.55×10^{-2}
3	2.50×10^{-1}	2.47×10^{-1}	2.55×10^{-3}	1.02×10^{-2}
4	2.00×10^{-1}	1.99×10^{-1}	1.45×10^{-3}	7.27×10^{-3}
5	1.67×10^{-1}	1.64×10^{-1}	2.49×10^{-3}	1.49×10^{-2}
6	1.43×10^{-1}	1.39×10^{-1}	3.77×10^{-3}	2.64×10^{-2}
7	1.25×10^{-1}	1.23×10^{-1}	1.70×10^{-3}	1.36×10^{-2}
8	1.11×10^{-1}	1.09×10^{-1}	2.61×10^{-3}	2.35×10^{-2}
9	1.00×10^{-1}	9.70×10^{-2}	3.01×10^{-3}	3.01×10^{-2}
10	9.09×10^{-2}	8.82×10^{-2}	2.74×10^{-3}	3.02×10^{-2}
11	8.33×10^{-2}	8.07×10^{-2}	2.65×10^{-3}	3.18×10^{-2}
12	7.69×10^{-2}	7.46×10^{-2}	2.36×10^{-3}	3.07×10^{-2}
13	7.14×10^{-2}	6.90×10^{-2}	2.41×10^{-3}	3.38×10^{-2}
14	6.67×10^{-2}	6.49×10^{-2}	1.77×10^{-3}	2.65×10^{-2}
15	6.25×10^{-2}	6.07×10^{-2}	1.83×10^{-3}	2.94×10^{-2}
16	5.88×10^{-2}	5.65×10^{-2}	2.30×10^{-3}	3.90×10^{-2}
17	5.56×10^{-2}	5.32×10^{-2}	2.31×10^{-3}	4.15×10^{-2}
18	5.26×10^{-2}	5.00×10^{-2}	2.58×10^{-3}	4.91×10^{-2}
19	5.00×10^{-2}	4.82×10^{-2}	1.80×10^{-3}	3.60×10^{-2}
Second Moments				
0	2.00×10^0	1.95×10^0	5.37×10^{-2}	2.69×10^{-2}
1	5.00×10^{-1}	4.75×10^{-1}	2.45×10^{-2}	4.91×10^{-2}
2	2.22×10^{-1}	2.23×10^{-1}	1.14×10^{-3}	5.12×10^{-3}
3	1.25×10^{-1}	1.23×10^{-1}	1.83×10^{-3}	1.47×10^{-2}
4	8.00×10^{-2}	7.91×10^{-2}	9.47×10^{-4}	1.18×10^{-2}
5	5.56×10^{-2}	5.40×10^{-2}	1.55×10^{-3}	2.79×10^{-2}
6	4.08×10^{-2}	3.80×10^{-2}	2.81×10^{-3}	6.90×10^{-2}
7	3.13×10^{-2}	3.00×10^{-2}	1.29×10^{-3}	4.13×10^{-2}
8	2.47×10^{-2}	2.30×10^{-2}	1.73×10^{-3}	7.02×10^{-2}
9	2.00×10^{-2}	1.84×10^{-2}	1.65×10^{-3}	8.25×10^{-2}
10	1.65×10^{-2}	1.48×10^{-2}	1.72×10^{-3}	1.04×10^{-1}
11	1.39×10^{-2}	5.44×10^{-3}	8.45×10^{-3}	6.09×10^{-1}
12	1.18×10^{-2}	1.07×10^{-2}	1.15×10^{-3}	9.74×10^{-2}
13	1.02×10^{-2}	7.04×10^{-3}	3.17×10^{-3}	3.11×10^{-1}
14	8.89×10^{-3}	8.25×10^{-3}	6.36×10^{-4}	7.16×10^{-2}
15	7.81×10^{-3}	4.83×10^{-3}	2.98×10^{-3}	3.82×10^{-1}
16	6.92×10^{-3}	6.09×10^{-3}	8.32×10^{-4}	1.20×10^{-1}
17	6.17×10^{-3}	5.21×10^{-3}	9.66×10^{-4}	1.56×10^{-1}
18	5.54×10^{-3}	3.79×10^{-3}	1.75×10^{-3}	3.15×10^{-1}
19	5.00×10^{-3}	3.65×10^{-3}	1.35×10^{-3}	2.70×10^{-1}

Table 2: Moment estimates for $d = 20$

References

- [1] JG Dai, Masakiyo Miyazawa, and Jian Wu. A multi-dimensional srbm: geometric views of its product form stationary distribution. *Queueing Systems*, 78(4):313–335, 2014.
- [2] Jose Blanchet, Xinyun Chen, Nian Si, and Peter W Glynn. Efficient steady-state simulation of high-dimensional stochastic networks. *Stochastic Systems*, 11(2):174–192, 2021.
- [3] Joseph Abate and Ward Whitt. A unified framework for numerically inverting laplace transforms. *INFORMS Journal on Computing*, 18(4):408–421, 2006.
- [4] Yanlin Qu, Jose Blanchet, and Peter Glynn. Deep learning for computing convergence rates of markov chains. *Advances in Neural Information Processing Systems*, 37:84777–84798, 2024.
- [5] Yanlin Qu, Jose Blanchet, and Peter Glynn. Deep learning for markov chains: Lyapunov functions, poisson’s equation, and stationary distributions. *Queueing Systems*, 110(1):10, 2026.
- [6] Jiequn Han, Arnulf Jentzen, et al. Deep learning-based numerical methods for high-dimensional parabolic partial differential equations and backward stochastic differential equations. *Communications in mathematics and statistics*, 5(4):349–380, 2017.
- [7] Jiequn Han, Arnulf Jentzen, and Weinan E. Solving high-dimensional partial differential equations using deep learning. *Proceedings of the National Academy of Sciences*, 115(34):8505–8510, 2018.
- [8] Baris Ata and Yaosheng Xu. Dynamic control of stochastic matching systems in heavy traffic: An effective computational method for high-dimensional problems. *arXiv preprint arXiv:2509.00809*, 2025.
- [9] Barış Ata and Ebru Kaşıkarcılar. Dynamic scheduling of a multiclass queue in the halfin–whitt regime: A computational approach for high-dimensional problems. *Management Science*, 2025.
- [10] Barış Ata, Wouter van Eekelen, and Yuan Zhong. A computational method for solving the stochastic joint replenishment problem in high dimensions. *arXiv preprint arXiv:2511.11830*, 2025.
- [11] Baris Ata, J Michael Harrison, and Nian Si. Drift control of high-dimensional reflected brownian motion: A computational method based on neural networks. *Stochastic Systems*, 15(2):111–146, 2025.
- [12] Baris Ata, J Michael Harrison, and Nian Si. Singular control of (reflected) brownian motion: A computational method suitable for queueing applications. *Queueing Systems*, 108(3):215–251, 2024.

- [13] E Weinan, Jiequn Han, and Arnulf Jentzen. Algorithms for solving high dimensional pdes: from nonlinear monte carlo to machine learning. *Nonlinearity*, 35(1):278, 2021.
- [14] Giuseppe Carleo and Matthias Troyer. Solving the quantum many-body problem with artificial neural networks. *Science*, 355(6325):602–606, 2017.
- [15] Bing Yu et al. The deep ritz method: a deep learning-based numerical algorithm for solving variational problems. *Communications in Mathematics and Statistics*, 6(1):1–12, 2018.
- [16] Justin Sirignano and Konstantinos Spiliopoulos. Dgm: A deep learning algorithm for solving partial differential equations. *Journal of computational physics*, 375:1339–1364, 2018.
- [17] Alan Talbot. The accurate numerical inversion of laplace transforms. *IMA Journal of Applied Mathematics*, 23(1):97–120, 1979.
- [18] Jacob Andre C Weideman. Optimizing talbot’s contours for the inversion of the laplace transform. *SIAM Journal on Numerical Analysis*, 44(6):2342–2362, 2006.
- [19] Joseph Abate and Ward Whitt. The fourier-series method for inverting transforms of probability distributions. *Queueing systems*, 10(1):5–87, 1992.
- [20] JG Dai and J Michael Harrison. Reflected brownian motion in an orthant: numerical methods for steady-state analysis. *The Annals of Applied Probability*, 2(1):65–86, 1992.
- [21] J Michael Harrison. The diffusion approximation for tandem queues in heavy traffic. *Advances in Applied Probability*, 10(4):886–905, 1978.
- [22] The mpmath development team. *mpmath: a Python library for arbitrary-precision floating-point arithmetic (version 1.4.0)*, 2026. <http://mpmath.org/>.
- [23] Gagan L Choudhury and David M Lucantoni. Numerical computation of the moments of a probability distribution from its transform. *Operations Research*, 44(2):368–381, 1996.